Kinetic Precipitation of Solution-Phase Polyoxomolybdate Followed by Transmission Electron Microscopy: A Window to Solution-Phase Nanostructure

Yan Zhu,[a] Arthur Cammers-Goodwin,*[a] Bin Zhao,[b] Alan Dozier,[c] and Elizabeth C. Dickey[d]

Abstract: This study aimed to elucidate the structural nature of the polydisperse, nanoscopic components in the solution and the solid states of partially reduced polyoxomolybdate derived from the $\{Mo_{132}\}$ keplerate, $\{(Mo)Mo_5\}_{12}$-$\{Mo_2$ acetate$\}_{30}$. Designer tripodal hexamine-tris-crown ethers and nanoscopic molybdate coprecipitated from aqueous solution. These microcrystalline solids distributed particle radii between 2–30 nm as assayed by transmission electron microscopy (TEM). The solid materials and their particle size distributions were snap shots of the solution phase. The mother liquor of the preparation of the $\{Mo_{132}\}$ keplerate after three days revealed large species ($r = 20$–30 nm) in the coprecipitate, whereas $\{Mo_{132}\}$ keplerate redissolved in water revealed small species (3–7 nm) in the coprecipitate. Nanoparticles of coprecipitate were more stable than solids derived solely from partially reduced molybdate. The TEM features of all material analyzed lacked facets on the nanometer length scale; however, the structures diffracted electrons and appeared to be defect-free as evidenced by Moiré patterns in the TEM images. Moiré patterns and size-invariant optical densities of the features in the micrographs suggested that the molybdate nanoparticles were vesicular.

Keywords: electron microscopy · molecular recognition · nanostructures · phase transitions · polyanions

Introduction

Polyoxometalates of early transition metals are structurally diverse.[1] In particular, physical and chemical properties of polyoxomolybdate has intrigued investigators for many years.[2] However, structural details of polymeric polyoxomolybdates waited two centuries to be elucidated by the solid-state studies of Müller and co-workers.

Arguably, the most intriguing oxometalate species are various closed-surface derivatives.[3] These structures highlight the fact that the closed surface is composed of discrete subunits. In the case of the $\{Mo_{132}\}$ keplerate,[4] the repeating structural motif is the pentagonal subunit, $(Mo)Mo_5$, linked at the edges by $\{Mo_2$ acetate$\}$ to form an I_h symmetric cluster. These nanoscale species carve out inner space with interesting internal solvent structure and they open the possibility of chemical reactions inside the closed surface.[5] Structural diversity in material related to $\{Mo_{132}\}$ keplerate includes discrete, nano-meso scale toroids and spheres arising from hierarchical assembly,[6] and the reduction of symmetry.[7] The diverse morphologies reported for the solid states invite speculation that media-dependent solution-state equilibria also involve multiple sizes and morphologies. The current work focuses on nanoscopic variants of the $\{Mo_{132}\}$ keplerate. This polymeric distribution of anions will be referred to as polypent-Mo_2.

Weight-average, size-average, and multi-modal distributions of particle sizes are available from dynamic laser light scattering (DLS) techniques. The large extinction coefficients of the $\{Mo_{132}\}$ keplerate and related structures hinder

[a] Dr. Y. Zhu, Prof. Dr. A. Cammers-Goodwin
University of Kentucky, Chemistry Department
Lexington, KY 40506-0055 (USA)
Fax: (+1) 859 323-1069
E-mail: a.cammers@uky.edu

[b] B. Zhao
University of California Riverside
Department of Chemistry, Riverside, CA 92521-0403 (USA)

[c] Dr. A. Dozier
University of Kentucky, Chemical and Materials Engineering
A004 ASTeCC Bldg, Lexington, KY 40506-0286 (USA)

[d] Prof. Dr. E. C. Dickey
Pennsylvania State University
Department of Materials Science and Engineering, 195 MRI Bldg.
University Park, PA 16802 (USA)

Supporting information for this article is available on the WWW under http://www.chemeurj.org/ or from the author. This includes full field views of the partial TEM images presented in the Figures. Selected NMR spectra of **1** and **2**.

 DOI: 10.1002/chem.200305468

DLS sizing of polypent-Mo_2 particles. However, enough data are available to conclude that polypent-Mo_2 in water is more size-disperse than polypent-Mo_2 in other solvent systems. DLS techniques gave good results with the relatively transparent, aqueous Fe derivative, of which the $\{Fe_{30}Mo_{72}\}$ keplerate is the smallest, discrete structure with a closed surface. The DLS studies indicate two-size regimes in solution and imply hollow structures for the nanoscale Fe–Mo polyoxometalate species.[8]

Ensemble sizing techniques such as DLS give averages of sizes, whereas non-ensemble techniques such as electron microscopy (EM) can highlight the properties of individual structures such as particle morphology and composition.[9] SEM (scanning) and TEM (transmission) have been applied to solids derived from polypent-Mo_2.[8a,10] The current study corroborates these results and adds new insights into the nature of polypent-Mo_2 solution states.

The current work develops a protocol for the kinetic precipitation of polypent-Mo_2 with chelating agents **1** and **2** to produce **ppt1** and **ppt2** (Figure 1). The preservation of solution-state conformation was also posited for an oligomeric polyelectrolyte. In that study, kinetic entrapment on surfaces followed by atomic force microscopy probed solution-phase folding.[11] The current study is also related to work involving complex formulations of polypent-Mo_2 material with surfactant in which the inorganic material forms ordered phases with less aggressive additives.[12]

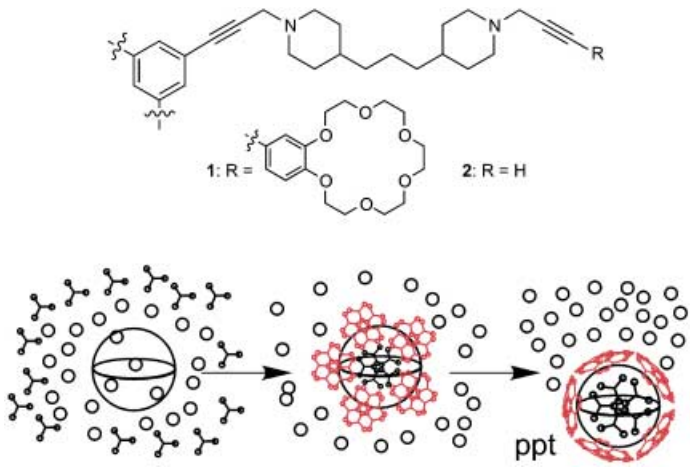

Figure 1. Top: tripodal molecules used to trap polypent-Mo_2; bottom: schematic representation of kinetic precipitation of polypent-Mo_2. The circles represent solvent; the triangles represent tripodal molecules **1**; and the large sphere represents nanoscale polypent-Mo_2 aqueous species. Kinetic solution state structure is preserved in the solid.

In the current study, large **ppt1** species derived from the mother liquor of the preparation of $\{Mo_{132}\}$ keplerate populated the micrographs. However, small species were found in **ppt1** generated from dissolved, crystalline $\{Mo_{132}\}$ keplerate. These two facts indicated that the distributions of particle sizes and morphologies of **ppt1** as revealed by TEM generated repeatable snap shots of polypent-Mo_2 in solution. Diamines related to crown **1** and to hexamine **2** did not succeed in trapping the polypent-Mo_2 solution state. Other tripodal structures related to **1** were less successful. This larger study will appear in doctoral thesis format.

To invoke kinetic precipitation, the phase transition from the solution state to the solid state must occur faster than structural changes in the material. From previous work, the dynamic structure in the solution state of chemically related species easily satisfies these conditions.[8a,13] The solubility of polypent-Mo_2 decreases with increasing ionic strength, presumably due to the destruction of the hydration shell.[14] Likewise, electrostatic interactions between the tripodal chelating agents (**1** or **2**) and polypent-Mo_2 should have cooperatively destroyed the hydration shell and led to an insoluble polypent-Mo_2 complex. The amines in **1** and **2** protonate below pH 7. Crown ethers associate with H_3O^+, NH_4^+ or K^+ and thereby can take on positive charges. In any surface-bound state, the positively charged benzocrown ethers in **1** would have to be proximal. Precedent exists for cation-associated crown ether moieties interacting favorably in the solid state.[15]

Results and Discussion

Material redissolved from the crystallization-driven preparation of the $\{Mo_{132}\}$ keplerate[3a] and material from the mother liquor was used in this study. In the TEM surveys in Figures 2 and 3, individual $\{Mo_{132}\}$ keplerate species ($r =$ 1.3 nm) probably merged with the granularity of the micrographs. Thus, it was much easier to image the larger, less popular species on which this study focused. The nanoscopic species derived from the mother liquors of the preparation (Figure 4A) were unambiguously larger than were those derived from the redissolved keplerate material (Figures 2 and 3). Thus, the time scale of coprecipitation was shorter than the solution-phase enlargement of nanoscopic species.

Samples for TEM analysis were prepared by three methods. These are described in detail in the first part of the experimental section. TEM analysis repeatedly revealed nanoscopic spherical features in **ppt1** whereas micrographs of **ppt2** were devoid of features with radii greater than 4 nm (compare Figures 2A, 3A, and 3B with 2B).

Ppt1 formed within seconds whereas the super-sized structures of aqueous state polypent-Mo_2 require two to three days to evolve. When a chemically related species is prepared fresh, small angle X-ray scattering (SAXS) does not detect particles in the solution phase with radii greater than 5 nm. After the material is allowed to stand for two days, SAXS analysis indicates the evolution of particles with sizes in the $r \sim 20$ nm range.[8a] One parameter that would have made kinetic precipitation of polypent-Mo_2 impossible would have been a fast chemical process that would have removed large polypent-Mo_2 particles from the distribution. The slow forward rate process for the evolution of nanostructured species guarantees a slower reverse process for the decomposition of the nanoscopic species. Slow assembly of nanoscopic species chemically related to the $\{Fe_{30}Mo_{72}\}$ keplerate has also been recently reported by Liu.[13]

Coprecipitates **ppt1** and **ppt2**, derived from polypent-Mo_2 and **1** or **2**, were very insoluble; titration of polypent-$Mo_{2(aq)}$

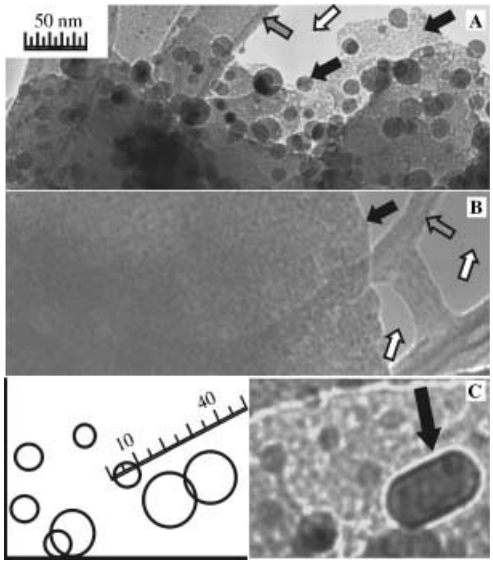

Figure 2. Micrographs of **ppt1** (A) and **ppt2** (B) formed upon addition of **1** or **2** respectively to polypent-Mo_2 in a 20:1 ratio. Analysis of the solid confirmed the 20:1 ratio of **1** (C, H, N elemental analysis) to total Mo by inductively coupled plasma atomic emission.[1b] Micrographs A and B have identical scale and magnification. Solids **ppt1** and **ppt2** were similar in appearance. Preparations of the solids for TEM were identical. Grey and white arrows indicate the lacey carbon substrate and voids respectively. The black arrows indicate material that contained Mo by energy dispersive X-ray spectroscopy. Ellipsoidal features were also located (C). These were probably structures in transition.

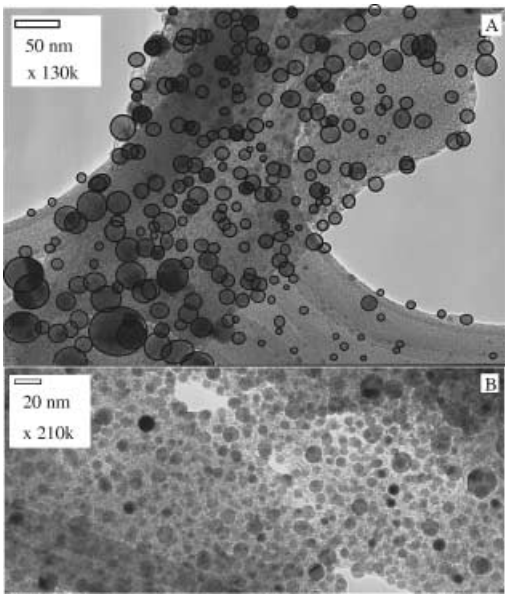

Figure 3. Micrographs from Method 1. Enclosures for measurement are drawn around features in A).

with excess **1** or **2** left little polypent-Mo_2 in solution detectable by UV at 455 nm, $\varepsilon = 1.85 \times 10^5\,\text{M}^{-1}\,\text{cm}^{-1}$ [1b] Tripodal **1** in 0.1 M KCl became soluble below pH 6 as determined by simultaneously decreasing the pH and monitoring the absorbance of the liquid at 290 nm. A titration monitored at 455 nm showed that polypent-Mo_2, 4.0×10^{-9} M,[1b] irreversibly decomposed above pH 6. In contrast, **ppt1** did not dissolve after agitation in water from pH 1–11 at room temperature.

The large features in **ppt1** decomposed over the course of 3–4 weeks into featureless material by TEM. The decomposed material resembled the Mo-containing material in Figure 2B (black arrow). In a few micrographs, the restructuring of the spherical features might have been caught on camera. Figure 2C shows a micrograph containing a rare elliptical feature that is approximately twice as long as it is wide (33×17 nm). With microscopy of lower resolution, this hypothesis for the observation of asymmetric transition structures was offered sixty years ago.[8a]

Species larger than those derived from the dissolution of crystalline Mo_{132} were observed in solids derived from the mother liquor of the preparation of Mo_{132} (Figure 4A–C). These were imaged as **ppt1** and as polypent-Mo_2, which linked the observations of nanostructure to polypent-Mo_2 and not to synergy between polypent-Mo_2 and **1**.

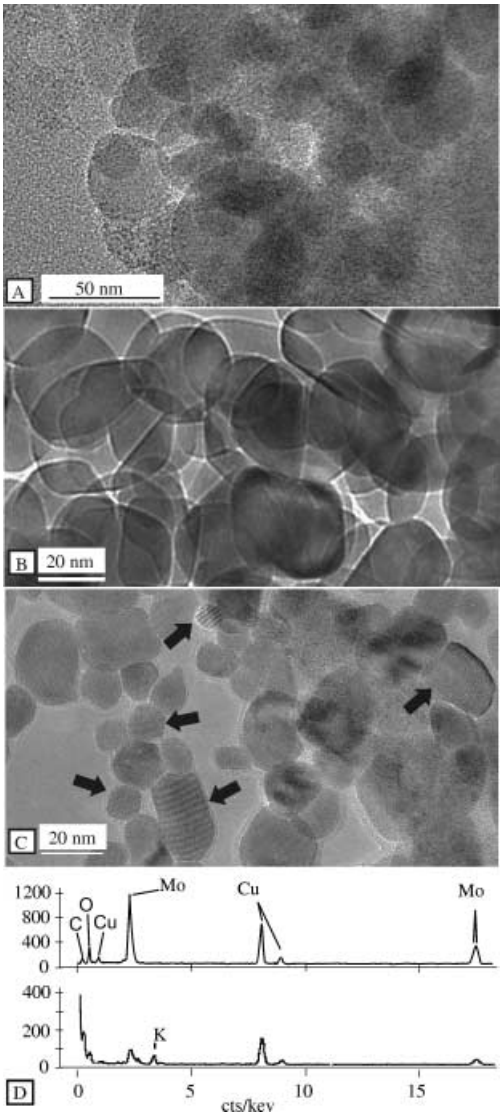

Figure 4. Solids from nanoscopic species in the mother liquor after 2–4 d. A) **ppt1**. B) TEM at magnification 120 k of polypent-Mo_2 by Method 2, dry preparation. C) TEM of polypent-Mo_2 by Method 3, wet preparation. D) Energy dispersive spectra of polypent-Mo_2 (top) and **ppt1** (bottom). The Cu grid produced the Cu peaks.

Ppt1 and polypent-Mo_2 differed in elemental content by energy dispersive X-ray spectra (EDS). Material absorbs high-energy electrons and releases X-rays with frequencies and intensities semi-quantitatively characteristic of elemental composition.[16] Figure 4D displays two representative EDS spectra of polypent-Mo_2 (top) and **ppt1** (bottom). The relative amount of Mo versus lighter elements in polypent-Mo_2, was lower than in **ppt1**. The benzocrown moiety in **1** presumably sequestered potassium from solution as evidenced by its detection in **ppt1**.

The features in the micrographs of **ppt1** produced ordered spot diffraction patterns, signaling a microcrystalline lattice in these objects. The diffraction pattern shown in Figure 5A had Bragg lattice spacing 1.1, 1.8, 2.2 and 4.2 Å. Most of the spacings in the spot diffraction pattern in Figure 5A were likely produced from high-Miller index phenomena, through the Mo-lattice of one or more nanoscale species. However, lattice spacing of 4.2 ± 0.4 Å matched Mo–Mo distances (~ 3.8 Å) in the X-ray structure of the $\{Mo\}_{132}$ keplerate.[17]

The micrographs were used to produce particle size distributions by measuring and counting the particles in the field with the aid of image processing software. Examples of the counting/measuring process are shown in Figures 2C and 3A in which boundaries were drawn around the features. In the image analysis, ellipses were mathematically fitted to the closed curves and evaluated statistically in terms of size, and circularity.

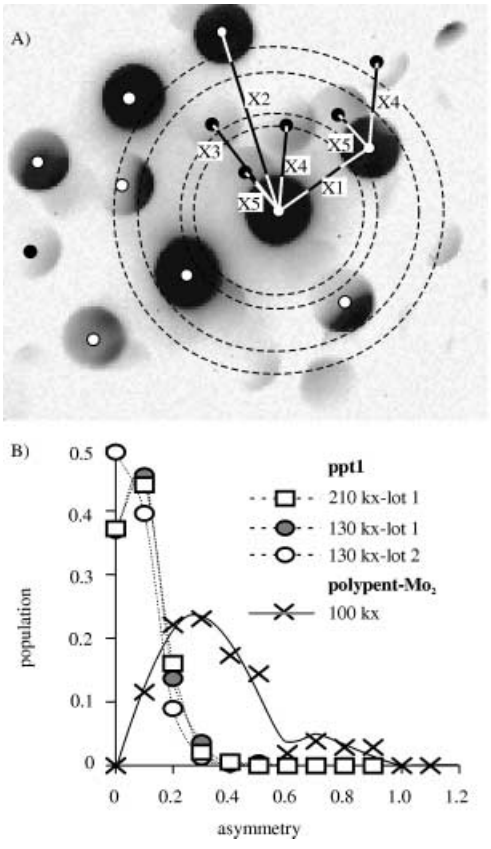

Figure 5. A) A spot diffraction pattern of a feature in Figure 2A that indicated that the Mo-atom lattice was intact in the superstructure. The superimposed dashed lines are a diffraction pattern produced by an Au calibration standard to determine the camera constant of the TEM. Segments X1-X5 correspond to lattice spacings 1.8, 1.1, 1.7, 2.2, 4.1 ± 0.4 Å, respectively. B) Plots the number of particles as a function of a unit-less asymmetry index: asymmetry = (long axis−short axis)/(average diameter) is the deviation from circularity of the feature normalized by its average size. When the index is zero, the feature is a perfect circle. One lot was analyzed at magnification 130 and 210 k; the asymmetry did not differ at these two magnifications.

The nanostructures in the micrographs of polypent-Mo_2 in the absence of tripodal molecules were not as circular as were those of **ppt1**; compare Figure 4A–C with Figures 2A and 3. Quantitatively, the ratio of anisotropic to spherical structures was higher in solid polypent-Mo_2 than in **ppt1** regardless of the source of the material. Figure 5B is a distribution of particle morphologies by the index function: asymmetry = (major axis−minor axis)/(average width). The structural anisotropy of the polypent-Mo_2 solid states probably corresponded to their decreased stability compared to **ppt1**. Asymmetry in these structures could have been due to the loss of solvent from the interior of the vesicles.

Figure 6A indicates that the TEM-derived particle size distributions of the dissolved crystalline material were skewed toward the size the smallest discrete closed structure, the keplerate. The resolution of these electron micrographs is ~2–3 nm, approximately the diameter of $\{Mo_{132}\}$ keplerate. Analyses of two samples of **ppt1** in Figure 6 at magnification 130 k and 210 k showed magnification-independent size distributions of polypent-Mo_2.

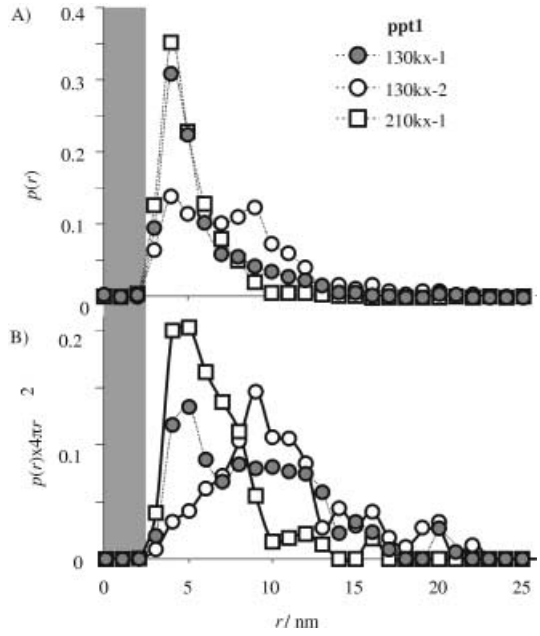

Figure 6. A) Magnification-independent distributions of particle sizes. B) Conversion of the data in A to mass distributions. The shaded line at left is the TEM resolution limit for particle selection and measurement. These graphs are not equilibrium distributions. The data sets generated at magnification 130 and 210 k were identical within experimental error.

Most experimental results scale with the mass distribution of the material instead of the number distribution of particles. For example, larger particles scatter light more efficiently, skewing the measurement toward larger values. An argument is presented below for hollow polypent-Mo_2 struc-

tures. Therefore, conversion of size distribution to mass distribution should employ the formula for the surface area of a sphere. The *i*th population element in the distribution is expressed as: $P(r)_i = 4\pi r^2 n_i/N$. The mass distribution, thus derived, is shown in 6B. The noise in the heavy region of the mass distribution is understandable when one considers that one large particle out of hundreds raised the graph off the zero line.

Particles derived from the solution phase (material adsorbed onto TEM grids) of the polypent-Mo_2 preparation[3a] were larger than were those derived from the soluble crystalline product. Compare average particles sizes in **ppt1** of the three graphs in Figure 6A, $r_{av} = 7 \pm 3$, 8 ± 4, and 5 ± 2 nm to the average sizes of two lots of the polypent-Mo_2 material, $r_{av} = 22 \pm 11$ and 32 ± 7 nm and a sample of **ppt1** derived from the preparative solution phase, $r_{av} = 20 \pm 5$ nm. Even though nanoscopic species found in **ppt1** derived from the mother liquor were larger than were those found in **ppt1** derived from Mo_{132}, they were no less symmetrical. The size distributions of the nanoscopic features in Figure 4A (r ~ 25 nm) were probably representative of a solution phase near equilibrium conditions. The less symmetric polypent-Mo_2 species in Figure 4B–C probably deformed because of loss of internal solvent molecules under the TEM vacuum. Neither their size nor morphology should be interpreted to reflect the solution state polypent-Mo_2.

The features in the micrographs above were hollow by two arguments presented in this paragraph and the one that follows. The morphologies of the polypent-Mo_2 in Figure 4B and C, and **ppt1** in Figures 2, 3 and 4A appear to be continuous and not constructed from units of $\{Mo\}_{132}$ keplerate. This smooth construction is exceptionally visible in Figure 4C which shows isolated nanoscopic features with Moiré patterns suggesting wave interference produced by two lattices each consisting of one or multiple layers. Isolated, solid, objects would not have produced these Moiré patterns.

In general, the optical densities of micrographic features scale with the atomic weight and the number of atoms encountered by the electron beam. Heavier and more numerous atoms scatter more electrons which gives rise to darker images. This maxim is most pertinent to objects in micrographs that weakly diffract electrons, the optical densities of which have weak angular dependencies on the electron beam. Figure 7 indicates that doubling the mass through which the electron beam passed detectably changed the optical density of the images. However, the optical densities of the features versus the radii of the features in the micrographs above were essentially constant in the TEM images. This effect is striking in Figure 4B, a micrograph with objects 4x larger than those in Figure 7, however, similar changes in optical densities in Figures 4B and 7 were noted when objects overlapped. Objects possessing radii from 3 to 30 nm were detected in the micrographs of this study. If the features were structurally homologous from surface to core, this range would have corresponded to a 1000-fold increase in mass. Optical densities independent of mass can only be met if the features in the TEM were either hollow or flat. Spherical structures with Mo at the surface are the best interpretation of the data. Hollow structures are in accordance with Liu's light scattering studies of solution states of nanoscopic species of $\{Fe_{30}Mo_{72}\}$ keplerate.[8,13]

Synthesis: The tripodal molecules used in this study were efficiently assembled with a Sonogishira coupling protocol to assemble chains on the aromatic hub.[18] The final step attached a benzocrown ether to the three terminal alkynes. The esoteric conditions shown in Figure 8 for the coupling were necessary to obtain a respectable yield. Sonogishira couplings with electron-rich aromatic substrates are known to cause difficulties; there is only one recent example of success with the commercial bromobenzocrown ether.[19] The tri-functionalization of compound **2** required an efficient process afforded by the iodo derivative.[20] For further details see the Experimental Section.

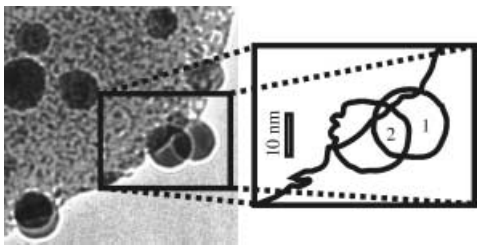

Figure 7. The weak dependence of optical density of objects on size suggested hollow structures. Imaged electrons scatter through one sphere in region 1 and two spheres in region 2. The grey scale value of region 1 is 13 versus 48 for region 2 (0 = black, 255 = white). The same effect was observed in polypent-Mo_2 in the absence of **1** (see Figure 4B).

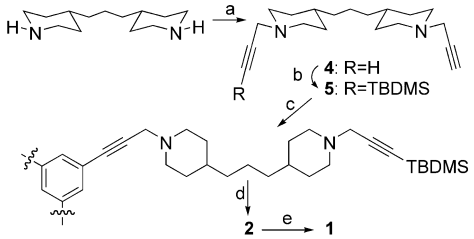

Figure 8. Synthetic overview: a) propargylbromide, NEt_3, THF; b) *n*BuLi/THF, then TBDMSCl, −78 °C; c) 1,3,5-tribromobenzene, $[Pd(PPh_3)_4]$, CuI, *n*$BuNH_2$, reflux, 72 h; d) TBAF/THF; e) 4-iodobenzocrown ether, $[Pd_2(dba)_3]$, tris-(2-furyl)phosphine, piperidine/DMF.

Conclusion

TEM studies of precipitates suggested smoothly constructed nanoscopic species in aqueous solution of polypent-Mo_2 instead of aggregates of $\{Mo\}_{132}$ keplerate. The independence of optical density on the size of the features in the micrographs, the lack of facets and uniform Moiré patterns in isolated objects indicated polysize-disperse, hollow polypent-Mo_2 in aqueous solution. The colloidal behavior of polypent-Mo_2 probably involves aggregation processes between nanoscale species. Effort was invested to avoid aggregation in this study with various levels of success.

This study developed a protocol to trap solution state structures of polypent-Mo_2. Future studies will involve attempts to characterize equilibria of nanoscale polypent-Mo_2 in solution and will include attempts to control distributions of sizes.

Experimental Section

ImageJ, Java freeware for image processing and statistical analysis, from (NIH, USA): http://rsb.info.nih.gov/ij/ was used to analyze image files generated from the TEM studies.

General synthetic methods: All reactions were carried out under Ar or N_2. THF was predried over CaH_2 and distilled from sodium/benzophenone. DMF was distilled from CaH_2 and stored over 4 Å molecular sieves under nitrogen. All the other reagents were used as received from commercial sources. ^{1}H NMR and ^{13}C NMR spectra were recorded at 400 and 100 MHz, respectively.

Solids for TEM analysis: All solids analyzed by TEM were derived from the published preparation of the $\{Mo_{132}\}$ keplerate.[3a] $N_2H_4{\cdot}H_2SO_4$ (0.8 g, 6.1 mmol) was added to a 250 mL aqueous solution of $(NH_4)_6Mo_7O_{24}{\cdot}4H_2O$ (5.6 g, 4.5 mmol) and ammonium acetate (12.5 g, 162.2 mmol) and stirred for 10 min. Aqueous acetic acid (50% vol, 83 mL) was added and the preparation stood in an open flask at 20 °C for four days. A crystalline reddish-brown material was filtered off. The dark filtrate was saved for further study. The crystalline material was washed with 90% ethanol$_{aq}$, absolute ethanol, diethyl ether, and finally air-dried at 25 °C. The IR, Raman and UV/Vis spectral data for the resulting material corresponded with the literature.[3a]

Ppt1: A precipitate formed immediately when material obtained above (3.0 mg) in deionized H_2O (2.0 mL) was prepared and immediately mixed with tripodal compound **1** (4.0 mg) in H_2O (3.0 mL, 0.1 M KCl_{aq}, pH ~ 3). Centrifugation followed by air-drying at 25 °C gave **ppt1**; **ppt2** was obtained analogously by using molecule **2**.

Ppt1′: Approximately 700 μL of the mother liquor of the published procedure[3a] were transferred to a 15 mL plastic centrifuge tube, and diluted to 1 mL with deionized water to give a reddish brown solution. A precipitate formed immediately upon mixing this solution with tripodal compound **1** (4.0 mg) dissolved in H_2O (3.0 mL, 0.1 M KCl_{aq}, pH ~ 3). Centrifugation followed by air-drying at 25 °C gave **ppt1′**.

Sample preparation for TEM analysis

Method 1: **Ppt1** (~1 mg) was dispersed in water in a small vial by sonicating for 30 min (Fisher Ultrasonic cleaner FS9) while cooling with ice. A drop of the dispersion was placed on a Lacey carbon copper grid (Lacey Carbon Type-A, Ted Pella, Inc.). After soaking the grid for 2 min, filter paper was used to absorb moisture. The grid was allowed to air dry at 25 °C and was subjected to high vacuum for 3 h before TEM analysis. TEM samples of **ppt1′** and **ppt2** were prepared analogously. The materials were examined using an Electron Microscope (JEOL JEM-2000FX) and JEOL JEM-2010F.

Method 2: The solid material filtered from the published procedure[3a] was crushed gently in weighing paper between the fingers. A Lacey carbon grid was sprinkled with a small amount of the dry material for TEM analysis.

Method 3: Approximately 10 μL fresh filtrate[3a] was placed on a Lacey carbon copper grid. After 2 min, the solution was filtered and the grid was allowed to air dry at 25 °C. The grid was examined by TEM.

Electron microscopy: The camera constant (CC) of the TEM was determined by adjusting the electron microscope to the same settings for the acquisition of the diffraction pattern in Figure 5 and creating a standard ring diffraction pattern Gold on "Holey" Carbon Film, Ted Pella Inc. product no. 613. The four rings in this sample correspond to four known lattice spacings: $CC = r(\text{ring})_n \times (d_n)$ for $n = 1$–4, $CC = 48.5 \pm 0.6$ mm Å. The patterns were superimposed and the lattice spacings in the nanostructure of **ppt1** were measured from the lengths of segments X_n: $d(X_n) = CC/X_n$.

***N,N′*-Di-(2-propynyl)-4,4′-trimethylenedipiperidine (4)**: Neat propargyl bromide (4.41 mL, 49.5 mmol) was added to commercial **3**, 4,4′-trimethylenedipiperidine (5.08 g, 24.1 mmol) in THF (50 mL). After the addition of Et_3N (14.9 mL), the resulting emulsion was stirred vigorously at 25 °C for 20 h. Diethyl ether, 10% HCl_{aq} 50 mL each were added to the reaction mixture, and the phases were separated. The aqueous phase was made basic (2 M NaOH, 30 mL) and extracted with diethyl ether (3 × 60 mL). The organic phase was dried over $MgSO_4$. The solvent was evaporated and the residue separated on silica gel flash chromatography (40–60% EtOAc/hexane gradient elution) gave a light yellow oil pure by NMR (2.90 g, 42%). ^{1}H NMR (400 MHz, $CDCl_3$, 25 °C, TMS): $\delta = 1.20$–1.34 (m, 12H; CH, CH_2 and axial piperidine CH_2), 1.68–1.72 (m, 4H; equatorial piperidine CH_2), 2.15–2.21 (m, 4H; axial CH_2-N), 2.24 (t, $^4J(H,H) = 2.4$ Hz, 2H; ≡CH), 2.86–2.90 (m, 4H; equatorial CH_2-N), 3.30 (d, $^4J(H,H) = 2.4$ Hz, 4H; propargyl CH_2); ^{13}C NMR (100 MHz, $CDCl_3$): $\delta = 23.8$, 32.2, 35.1, 36.6, 47.2, 52.6, 73.1, 78.9; MS (70 eV, EI): *m/z* (%): 285 (11) $[M^+ - H]$, 247 (100) $[M^+ - C_3H_3]$; elemental analysis calcd (%) for $C_{19}H_{30}N_2$ (286.5): C 79.66, H 10.56, N 9.78; found: C 79.27, H 10.88, N 9.69.

***N*-(*tert*-Butyldimethylsilyl-2-propynyl)-*N′*-(2-propynyl)-4,4′-trimethylenedipiperidine (5)**: *n*-Butyllithium (14.6 mL, 29.2 mmol) was added dropwise to a THF solution of **4** (8.35 g, 29.2 mmol, −78 °C, in 100 mL THF) and kept cold for 30 min followed by dropwise addition of TBDMSCl (4.40 g, 29.2 mmol in 40 mL THF). The vessel was allowed to warm to 25 °C overnight. The solvent was evaporated and the resulting slurry was dispersed in biphasic diethyl ether and water; the phases were separated and the aqueous phase was extracted with ether, the combined organic phase was dried over $MgSO_4$. Flash chromatography on silica gel (20–60% EtOAc/hexane gradient) gave the title compound as a colorless oil (4.67 g, 40%). ^{1}H NMR (400 MHz, $CDCl_3$, 25 °C, TMS): $\delta = 0.10$ (s, 6H; Si-CH_3), 0.94 (s, 9H; C-CH_3), 1.20–1.34 (m, 12H; CH, CH_2 and axial piperidine CH_2), 1.68–1.72 (m, 4H; equatorial piperidine CH_2), 2.13–2.20 (m, 4H; axial CH_2-N), 2.23 (t, $^4J(H,H) = 2.3$ Hz, 1H; ≡CH), 2.83–2.90 (m, 4H, equatorial CH_2-N), 3.28 (d, $^4J(H,H) = 2.3$ Hz, 2H; propargyl CH_2), 3.33 (s, 2H; propargyl CH_2); ^{13}C NMR (100 MHz, $CDCl_3$): $\delta = -4.6$, 16.5, 23.9, 26.1, 26.1, 31.9, 32.1, 35.1, 36.5, 36.6, 47.2, 48.1, 52.3, 52.6, 73.1, 73.2, 78.8; MS (70 eV, EI): *m/z* (%): 400 (12) $[M^+]$, 361 (77) $[M^+ - C_3H_3]$, 343 (25) $[M^+ - C_4H_9]$, 285 (41) $[M^+ - C_6H_{15}Si]$, 247 (100) $[M^+ - C_9H_{17}Si]$; elemental analysis calcd (%) for $C_{25}H_{44}N_2Si$ (400.7): C 74.93, H 11.07, N 6.99; found: C 74.87, H 11.17, N 7.07.

1,3,5-Tris-[*N′*-(*tert*-butyldimethylsilyl-2-propynyl)-4,4′-trimethylenedipiperidino-*N*-(2-propyn-3-yl)]benzene (6): 1,3,5-Tribromobenzene (0.99 g, 3.145 mmol) and **5** (4.155 g, 10.38 mmol) was dissolved in *n*-butylamine (40 mL). The resulting solution was treated with $[Pd(PPh_3)_4]$ (0.363 g, 0.314 mmol) and CuI (0.12 g, 0.630 mmol) and the solution was heated under reflux for 72 h. After cooling to 25 °C, the solvents were evaporated and the residue was extracted into EtOAc, the organic phase was washed with water and brine and dried over $MgSO_4$. Flash chromatography on silica gel (gradient elution: 50–100% EtOAc/hexane followed by 2–8% MeOH/$CHCl_3$) give a yellow oil (3.0 g, 75%). ^{1}H NMR (400 MHz, $CDCl_3$, 25 °C, $CDCl_3$): $\delta = 0.11$ (s, 18H; Si-CH_3), 0.94 (s, 27H; C-CH_3), 1.22–1.38 (m, 36H; CH, CH_2 and axial piperidine CH_2), 1.71–1.75 (m, 12H; equatorial piperidine CH_2), 2.25 (dd, $^3J(H,H) \sim 11.5$, $^2J(H,H) = 11.5$ Hz, 6H; axial CH_2-N), 2.30 (dd, $^3J(H,H) \sim 11.5$, $^2J(H,H) = 11.5$ Hz, 6H; axial CH_2-N), 2.91 (d, $^2J(H,H) = 11.5$ Hz, 6H; equatorial CH_2-N), 2.97 (d, $^2J(H,H) = 11.5$ Hz, 6H; equatorial CH_2-N), 3.40 (s, 6H; propargyl CH_2), 3.51 (s, 6H; propargyl CH_2), 7.42 (s, 3H; CH aromatic); MS (MALDI-TOF): *m/z* (%): 1275 (100) $[M^+ + H]$.

1,3,5-Tris-[*N′*-(2-propynyl)-4,4′-trimethylenedipiperidino-*N*-(2-propyn-3-yl)]benzene (2): Compound **6** (2.28 g, 1.79 mmol) in 20 mL THF at 0 °C, was treated with TBAF (6.5 mL, 1 M, dropwise); the reaction mixture was stirred at 0 °C for 10 min, and then stirred at room temperature for 4 h. After quenching with NH_4Cl_{aq}, extracting into $CHCl_3$, and washing with water, the $CHCl_3$ phase was dried over Na_2SO_4. Flash chromatography on silica gel (gradient elution: 3–8% MeOH/$CHCl_3$) yielded a hygroscopic residue (1.4 g, 84%). ^{1}H NMR (400 MHz, $CDCl_3$, 25 °C, TMS): $\delta = 1.21$–1.36 (m, 36H; CH, CH_2 and axial piperidine CH_2), 1.68–1.74 (m, 12H; equatorial piperidine CH_2), 2.13–2.20 (m, 12H; axial CH_2-N), 2.23 (t, $^4J(H,H) = 2.4$ Hz, 3H; ≡CH), 2.87 (d, $^2J(H,H) = 11.5$ Hz, 6H; equatorial CH_2-N), 2.94 (d, $^2J(H,H) = 11.5$ Hz, 6H; equatorial CH_2-N), 3.28 (d, $^4J(H,H) = 2.4$ Hz, 6H; propargyl CH_2), 3.47 (s, 6H; propargyl CH_2), 7.40

(s, 3H; CH aromatic); ^{13}C NMR (100 MHz, $CDCl_3$): $\delta = 23.9$, 32.3, 32.4, 35.2, 35.2, 36.66, 36.68, 47.2, 48.0, 52.7, 53.0, 72.8, 79.2, 83.5, 86.2, 123.7, 134.2; MS (MALDI-TOF): *m*/*z* (%): 932.5 (100) $[M+H]^+$; elemental analysis calcd (%) for $C_{63}H_{90}N_6{\cdot}2H_2O$ (967.5): C 78.21, H 9.79, N 8.69; found: C 78.47, H 9.76, N 8.80.

1,3,5-Tris-[*N*′-(4′-benzo-18-crown[6])-2-propynyl)-4,4′-trimethylenedipiperidino-*N*-(2-propyn-3-yl)]benzene (1): $[Pd_2(dba)_3]$ (7.9 mg, 8.6 μmol) and CuI (1.6 mg, 8.4 μmol) and tris-(2-furyl)phosphine (4.1 mg, 17.6 μmol) were added to a dry, 5 mL septum-capped round flask, which was then sparged with argon and charged with dry DMF (0.5 mL). Neat piperidine (32 μL, 323 μmol) and 4′-iodobenzo-18-crown[6] (124 mg, 283 μmol, dissolved in 1.5 mL DMF) were added via syringe to the stirred reaction mixture. The resulted mixture stirred for 15 min at 25 °C, then compound **2** (80 mg, 86 μmol, dissolved in 1 mL DMF) was added dropwise via syringe in a period of 20 min. The whole reaction mixture was stirred at 25 °C. for 24 h. Then the resulted solid was filtered, the solvent was concentrated and the residue was purified by alumina column chromatography (gradient elution: EtOAc followed by 2–5% MeOH/$CHCl_3$), which yielded a yellow hygroscopic solid (120 mg, 75%). ^{1}H NMR (400 MHz, $CDCl_3$, 25 °C, TMS): $\delta = 1.18$–1.34 (m, 36H; CH, CH_2 and axial piperidine CH_2), 1.66–1.80 (m, 12H; equatorial piperidine CH_2), 2.14–2.22 (m, 12H; axial CH_2-N), 2.95 (t, $^2J(H,H) = 11.8$ Hz, 12H; equatorial CH_2-N), 3.45 (s, 6H; propargyl CH_2), 3.47 (s, 6H; propargyl CH_2), 3.69 (s, 12H; O-$(CH_2)_2$-O), 3.70–3.73 (m, 12H; CH_2-O), 3.76–3.78 (m, 12H; CH_2-O), 3.90–3.93 (m, 12H; CH_2-O), 4.12–4.16 (m, 12H; CH_2-O), 6.78 (d, $^3J(H,H) = 8.28$ Hz, 3H; CH aromatic benzocrown), 6.95 (d, $^4J(H,H) = 2.00$ Hz, 3H; CH aromatic benzocrown), 7.01 (dd, 3H, $^3J(H,H) = 8.28$ Hz, $^4J(H,H) = 2.00$ Hz, 3H; CH aromatic benzocrown), 7.40 (s, 3H; CH aromatic); ^{13}C NMR (100 MHz, $CDCl_3$): $\delta = 23.9$, 32.4, 35.25, 35.30, 36.7, 48.0, 48.2, 53.0, 53.1, 69.0, 69.5, 70.8, 70.9, 83.5, 83.6, 84.8, 86.2, 113.5, 115.9, 117.2, 123.7, 125.3, 134.2, 148.4, 149.2; MS (MALDI-TOF): *m*/*z* (%): 1863 (88) $[M+H]^+$, 1885 (100) $[M+Na]^+$; elemental analysis calcd (%) for $C_{111}H_{156}N_6O_{18}{\cdot}4H_2O$ (1934.6): C 68.92, H 8.13, N 4.34; found: C 69.02, H 8.26, N 4.42.

Acknowledgement

The authors thank Gerald Thomas of the Center for Applied Energy Research at the University of Kentucky for ICP analysis and the National Science Foundation, USA CHE0111578 for supporting this work. TEM and NMR support acknowledge NSF (USA), EPS-9874764 and CHE997841.

[1] a) M. T. Pope, in *Comprehensive Coordination Chemistry, Vol. 3* (Eds.: G. Wilkinson, R. D. Gillard, J. A. McCleverty), Pergamon Press, **1987**, pp. 1023–1058; the {Mo_{132}} keplerate is the smallest structure with a closed surface found in solid states of PPMo2AcO; {Mo_{132}} keplerate was used as a convenient basis for the concentration of molybdate in these studies.

[2] a) A. Müller, J. Meyer, E. Krickemeyer, E. Diemann, *Angew. Chem.* **1996**, *108*, 1296; *Angew. Chem. Int. Ed.* **1996**, *35*, 1206; b) P. Souchay, *Polyanions et polycations*, Oauthier-Villars, **1963**; c) W. D. Treadwell, Y. Schaeppi, *Helv. Chim. Acta* **1946**, *29*, 771; d) O. Glemser, G. Lutz, *Z. Anorg. Allg. Chem.* **1951**, *264*, 17.

[3] a) A. Müller, E. Krickemeyer, H. Bögge, M. Schmidtmann, F. Peters, *Angew. Chem.* **1998**, *110*, 3567; *Angew. Chem. Int. Ed.* **1998**, *37*, 3359; b) A. Müller, J. Meyer, E. Krickemeyer, C. Beugholt, H. Bögge, F. Peters, M. Schmidtmann, P. Kögerler, M. J. Koop, *Chem. Eur. J.* **1998**, *4*, 1000.

[4] The prepartion and crystallization of this material is an undergraduate exercise. L. Cronin, E. Diemann, A. Müller, in *Inorganic Experiments* (Ed.: J. D. Woollins), Wiley-VCH, Weinheim, **2003**, p. 340.

[5] A. Müller, E. Krickemeyer, H. Bögge, M. Schmidtmann, B. Botar, M. O. Talismanova, *Angew. Chem.* **2003**, *115*, 2131; *Angew. Chem. Int. Ed.* **2003**, *42*, 2085.

[6] a) A. Müller, S. S. Q. N. Sarkar, H. Bogge, M. Schmidtmann, S. Sarkar, P. Kogerler, B. Hauptfleisch, A. X. Trautwein, V. Schunemann, *Angew. Chem.* **1999**, *111*, 3435; *Angew. Chem. Int. Ed.* **1999**, *38*, 3238; b) A. Müller, P. Kögerler, H. Bögge, *Struct. Bonding* **2000**, *96*, 203.

[7] A. Müller, E. Diemann, S. Q. N. Shah, C. Kuhlmann, M. C. Letzel, *Chem. Commun.* **2002**, 440.

[8] a) A. Müller, E. Diemann, C. Kuhlmann, W. Eimer, C. Serain, T. Tak, A. Knöchel, P. K. Pranzas, *Chem. Commun.* **2001**, 1928; b) T. Liu, *J. Am. Chem. Soc.* **2002**, *124*, 10942.

[9] R. Xu, *Particle Characterization: Light Scattering Methods Particle Technology Series* (series Ed.: B. Scarlett), Kluwer, **2001**.

[10] a) F. B. J. Schinner, L. F. Audrieth, S. T. Gross, D. S. McClellan, L. J. Seppi, *J. Am. Chem. Soc.* **1942**, *64*, 2543; b) T. Liu, Q. Wan, Y. Xie, C. Burger, L.-Z. Liu, B. Chu, *J. Am. Chem. Soc.* **2001**, *123*, 10966.

[11] A. Kiriy, G. Gorodyska, S. Minko, W. Jaeger, P. Stepánek, M. Stamm, *J. Am. Chem. Soc.* **2002**, *124*, 13454.

[12] a) S. Palarz, B. Smarsly, M. Antonietti, *ChemPhysChem* **2001**, 457; b) D. G. Kurth, P. Lehmann, D. Volkmer, H. Cölfen, M. J. Koop, A. Müller, A. Du Chesne, *Chem. Eur. J.* **2000**, *6*, 385; c) D. Volkmer, A. Du Chesne, D. G. Kurth, H. Schnablegger, P. Lehmann, M. J. Koop, A. Müller *J. Am. Chem. Soc.* **2000**, *122*, 1995.

[13] T. Liu, *J. Am. Chem. Soc.* **2003**, *125*, 312.

[14] A. Müller, M. Koop, H. Bogge, M. Schmidtmann, C. Beugholt, *Chem. Commun.* **1998**, 1501.

[15] K. C. V. Sharma, A. Clearfield, *J. Am. Chem. Soc.* **2000**, *122*, 1558.

[16] a) J. C. Russ, *Fundamentals of energy dispersive X-ray analysis*, Butterworths, **1984**; b) B. Dziunikowski, *Energy dispersive X-ray fluorescence analysis*, Elsevier, **1989**.

[17] When the ring in the Au standard corresponding to Miller index [1.1.1] was used, the lattice spacing was 3.8 Å. The X-ray structure of {Mo_{132}} keplerate (CSD-410097, Fachinformationszentrum Karlsruhe, CRYSDATA@FIZ-Karlsruhe.DE) has Mo–Mo distances 3.80 Å (180×), 3.30 Å (60×) and 2.61 Å (30×).

[18] a) K. Sonogashira in *Metal-Catalyzed Cross-Coupling Reactions* (Eds.: F. Diederich, P. J. Stang), Wiley-VCH, New York, **1998**, p. 203; b) K. Sonogashira in *Comprehensive Organic Synthesis* (Eds.: B. M. Trost, I. Flemming), Pergamon, New York, **1991**, p. 521.

[19] W.-S. Xia, R. H. Schmehl, C.-J. Li, *Tetrahedron* **2000**, *56*, 7045.

[20] S. Kajigaeshi, T. Kakinami, M. Moriwaki, M. Watanabe, S. Fujisaki, T. Okamoto, *Chem. Lett.* **1988**, 795.

Received: August 20, 2003 [F5468]

Published online: March 22, 2004

